POLAR PLUME ANATOMY: RESULTS OF A COORDINATED OBSERVATION

C. E. DeFOREST[1], J. T. HOEKSEMA[1], J. B. GURMAN[2], B. J. THOMPSON[3], S. P. PLUNKETT[4,*], R. HOWARD[4], R. C. HARRISON[5] and D. M. HASSLER[6,†]
[1]*W.H. Hansen Experimental Physics Laboratory, Center for Space Science and Astrophysics, Stanford University, Stanford, CA 94305–4085, U.S.A.*
[2]*NASA/Goddard Space Flight Center, Greenbelt, MD 20771, U.S.A.*
[3]*Applied Research Corporation, U.S.A.*
[4]*E.O. Hurlbut Center for Space Research, Naval Research Laboratory Washington, DC 20375, U.S.A.*
[5]*Rutherford Appleton Laboratory, U.S.A.*
[6]*High Altitude Observatory, Boulder, CO, U.S.A.*

(Received 18 March 1997; accepted 18 June 1997)

Abstract. On 7 and 8 March 1996, the SOHO spacecraft and several other space- and ground-based observatories cooperated in the most comprehensive observation to date of solar polar plumes. Based on simultaneous data from five instruments, we describe the morphology of the plumes observed over the south pole of the Sun during the SOHO observing campaign. Individual plumes have been characterized from the photosphere to approximately 15 $R_\odot$, yielding a coherent portrait of the features for more quantitative future studies. The observed plumes arise from small ($\sim$2–5 arc sec diameter) quiescent, unipolar magnetic flux concentrations, on chromospheric network cell boundaries. They are denser and cooler than the surrounding coronal hole through which they extend, and are seen clearly in both Fe IX and Fe XII emission lines, indicating an ionization temperature between $1.0-1.5 \times 10^6$ K. The plumes initially expand rapidly with altitude, to a diameter of 20–30 Mm about 30 Mm off the surface. Above 1.2 $R_\odot$, plumes are observed in white light (as 'coronal rays') and extend to above 12 $R_\odot$. They grow superradially throughout their observed height, increasing their subtended solid angle (relative to disk center) by a factor of $\sim$10 between 1.05 $R_\odot$ and 4–5 $R_\odot$, and by a total factor of 20–40 between 1.05 $R_\odot$ and 12 $R_\odot$. On spatial scales larger than 10 arc sec, plume structure in the lower corona ($R < 1.3\ R_\odot$) is observed to be steady-state for periods of at least 24 hours; however, on spatial scales smaller than 10 arc sec, plume XUV intensities vary by 10–20% (after background subtraction) on a time scale of a few minutes.

1. Introduction

Polar plumes are linear structures that are apparent over the solar poles in visible light (e.g., Saito, 1965; Koutchmy, 1977), in extreme ultraviolet (e.g., Bohlin, Sheeley, and Tousey, 1975; Walker *et al.*, 1988, 1993), and in soft X-rays (e.g., Ahmad and Webb, 1978). They are thought to be denser than the surrounding media, and have been shown to diverge superradially with altitude (Ahmad and Withbroe, 1977; Fisher and Guhathakurta, 1995). While some observations (Harvey, 1965; Newkirk and Harvey, 1968; Lindblom, 1990; Allen, 1994) have suggested that polar plumes land on unipolar magnetic structures, the prevailing model has been

[*] Dr Plunkett is employed by the Universities Space Research Association.
[†] Dr Hassler is now employed by Southwest Research Institute, Boulder, CO.

Solar Physics **175:** 393–410, 1997.
© 1997 *Kluwer Academic Publishers. Printed in Belgium.*

one with small dipoles at the footpoints (e.g., Ahmad and Withbroe, 1977; Habbal, 1992; Saito, 1965). The relation of the polar plumes to the solar wind has been in dispute: some authors (e.g., Walker, 1990) believe that the plumes are a likely source for the high speed solar wind; while others (e.g., Habbal, 1992) believe otherwise.

The SOHO observing campaign of 7 and 8 March 1996 was the most comprehensive observation of polar plumes to date. The observation was designed to obtain a complete picture of the morphology of the plumes, from photospheric footpoint to outer corona; to provide plasma diagnostics to constrain semi-empirical plume and solar wind models; and to identify possible heating mechanisms – in particular, small-scale magnetic reconnection and MHD waves in the 2–10-min frequency band. For descriptions of the participating SOHO instruments, refer to Fleck, Domingo, and Poland (1995).

Figure 1 diagrams the observation plan that was used for all participating SOHO instruments and one of the ground-based observatories. The Michelson Doppler Imager ('MDI') recorded magnetic and Doppler information with 0.6 arc sec resolution and 1-min cadence; the Coronal Diagnostic Spectrometer ('CDS') observed the chromospheric roots of the plumes in He I, O V, and Mg IX spectral lines (intensity only) with a 1-min cadence; the EUV Imaging Telescope ('EIT') generated 3-min-cadence XUV images of the coronal hole in Fe IX/X and He II line emissions; the Solar Ultraviolet Measurement of Emitted Radiation spectrometer ('SUMER') rapidly scanned across the edge of a single observed plume to record differences in the O VI and Mg IX line profiles within and outside the plume; the UltraViolet Coronal Spectrometer ('UVCS') recorded Doppler dimming information and high cadence Lyα and O VI spectra across the hole at a single altitude (1.8 $R_\odot$) to obtain outflow rates and detect possible wave motions; and the Large Angle Spectrometric COronagraph ('LASCO') recorded still images of the middle and outer corona with its C2 and C3 coronagraphs before and after the bulk of the observations. Daily average images from the White-Light Coronagraph Mk 3 ('Mk 3') at HAO's Mauna Loa Solar Observatory were also incorporated into the SOHO data set.

In this paper, we concern ourselves primarily with a complete description of the directly observable parameters of the observed plumes. We use EIT, Mk 3, and LASCO to trace the plumes' morphology; CDS to identify the location of individual plumes' footpoints relative to the chromopheric network; and MDI for information on the magnetic structure of the plumes' lower reaches. As instrument calibrations become available, the EIT and LASCO data will be used in future analyses to extract density as a function of height in the plumes, while SUMER and UVCS data will be used to search for signatures of wave heating and plasma acceleration at moderate and high altitudes.

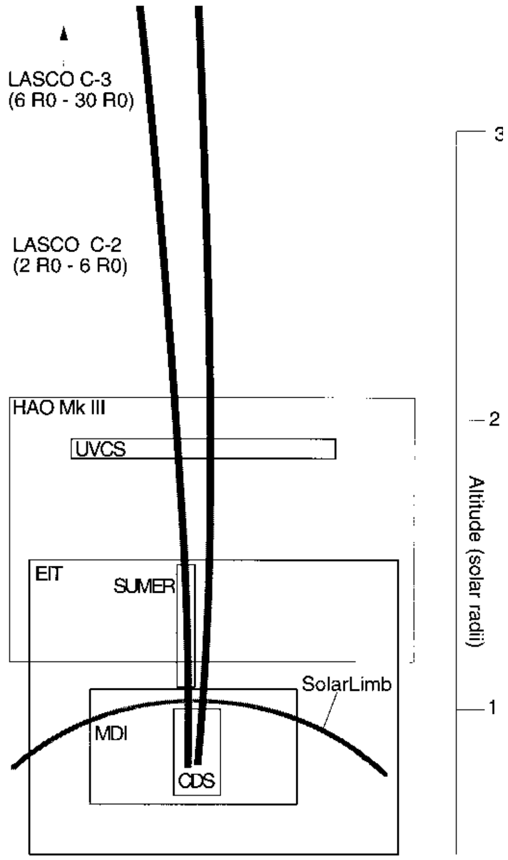

Figure 1. Schematic diagram of the SOHO March 1996 plume observation. Each instrument's field of view is marked, roughly (but not exactly) to scale. Because the LASCO fields of view are large compared to the disk, they are not drawn (only notated). MDI, CDS, EIT, SUMER, and UVCS each generated data at cadences of 1–4 min; the outer coronagraphs recorded single images before and after the bulk of the campaign observations.

2. Observations

2.1. EIT: POLAR PLUMES IN EUV/XUV

EIT (Delaboudinière *et al.*, 1995) recorded images of the south pole in the EUV/XUV portion of the spectrum for most of the observation, affording views of plume morphology and evolution in the lowest reaches of the corona. Because the off-point maneuver of the plumes campaign required LASCO to close its front aperture doors, all of the telemetry bandwidth normally allocated to LASCO was available to EIT. This in turn allowed EIT to record solar images with a much higher cadence, and a longer duration, than is normally possible. EIT's principal observations were a five-hour-long sequence of exposures at 171 Å (Fe IX/X) with

3-min time resolution from ∼16:30 UT to ∼21:30 UT on 7 March; a slightly shorter (2.5 hour) sequence of images at 304 Å (He II) starting at 7 March 07:22 UT; and several sets of full-disk exposures that cycle through the four available passbands. The plumes are readily visible in the Fe IX/X (171 Å) movie and the Fe XII (193 Å) images; they are less visible (but still apparent) in the Fe XV (284 Å) exposures, and do not appear in the He II (304 Å) images.

Figure 2 shows two images of the coronal hole taken 5 min apart: one in the 171 Å (Fe IX/X) passband, which is sensitive to plasma near 1.0×10^6 K; the other in the 195 Å (Fe XII) passband, which 'sees' plasma at temperatures of about 1.6×10^6 K. The plumes visible in Fe IX/X can be described as roughly linear features that subtend about 2.5° relative to Sun center as they cross the limb. The observed plumes appear to expand radially from a radiant that is between Sun center and the limb of the Sun, following the observations of Fisher and Guhathakurta (1995). However, the base of the plume can best be described as a 'blunt pencil' shape, suggestive of Newkirk and Harvey's (1968) model of magnetic flux near plume footpoints. Each plume arises from a small (2–4 Mm; ∼4 arc sec) footpoint and expands rapidly with height before assuming its characteristic slow expansion at about 20–30 Mm off the surface (with a diameter of about 20–30 Mm at that altitude).

While calculation of ionization temperatures from this dataset must wait for the final intensity calibration for EIT, one may draw some conclusions from the uncalibrated data. With the assumption that each plume is approximately isothermal across its width, one may conclude that the plume temperatures are between about $1.0–1.5 \times 10^6$ K: otherwise, they would be clearly visible in one or the other, but not both, of the images in Figure 2. This is because the Fe XII telescope is not sensitive to plasmas under about 1.0×10^6 K and the Fe IX/X telescope is not sensitive to plasmas above about 1.5×10^6 K. Furthermore, one may determine qualitatively which regions are hotter than others by comparing the relative brightnesses of features in the Fe IX/X and Fe XII passbands: hotter structures emit proportionally more light from the higher ionization state.

Figure 3 is a composite image of the two panels in Figure 2: its pixel values are calculated by dividing the Fe XII intensity by the Fe IX/X intensity, to show a rough temperature map. Most of the plumes appear darker than the surrounding media, indicating proportionally less 195 Å emission than 171 Å emission, or a lower ionization temperature than their surrounding media. Because the surrounding media are also visible in both passbands, the temperatures of both the interplume hole and the plumes themselves must be in the $1.0–1.5 \times 10^6$ K range; hence, the plumes are cooler than the background by up to (but not more than) 30%.

The result that plumes are relatively cool is consistent with scale height measurements made by Walker *et al.* (1993) from a 1987 XUV rocket observation, which showed a slightly higher scale height in the interplume regions than in plumes themselves in Fe IX/X emission; with recent observations of line width in O VI plumes by SUMER (Hassler *et al.*, 1997), wherein the O VI spectral line was

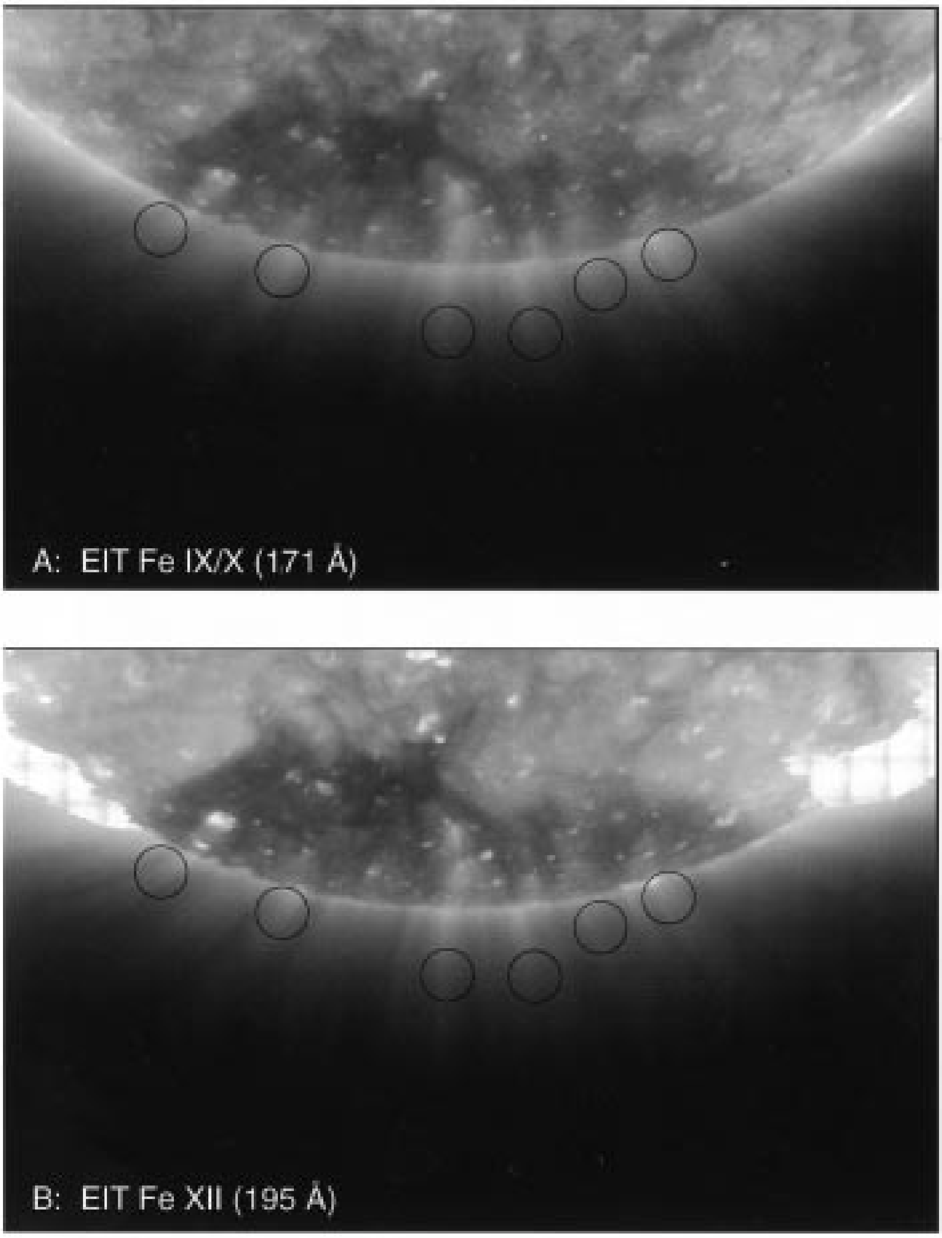

Figure 2. (A) The EIT Fe IX/X (171 Å) image from 16:45 UT, 7 Marrch 1996, showing polar plumes over the south polar hole at 1.0×10^6 K. (B) The EIT Fe XII (195 Å) image from 16:34 UT, 7 March 1996. This passband is sensitive to plasmas at 1.6×10^6 K. Some key locations have been circled for intercomparison between the two images.

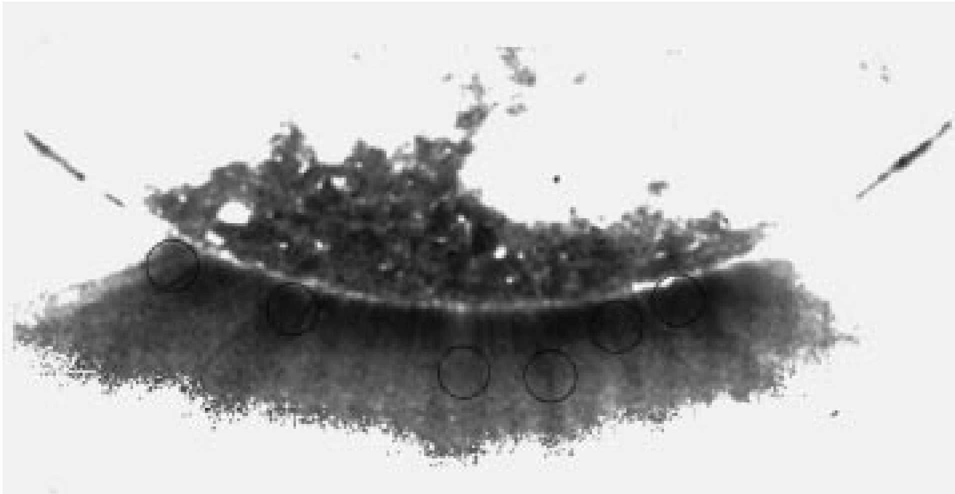

Figure 3. EIT ratio image: this image is a ratio of the two images in Figure 2, showing plasma temperature variations. Briqht features are proportionally brighter in Fe XII than in Fe IX, indicating higher temperature; dark features are proportionally dimmer in Fe XII than in Fe IX, indicating lower temperature. This ratio is sensitive over a range of about $0.9-1.8 \times 10^6$ K. All but two of the marked plumes appear dark in this image, indicating that they are somewhat cooler than the surrounding interplume background.

found to be narrower in plumes than in the interplume region; and with predictions made by Wang (1994). Walker *et al.* (1993) found plumes to have densities of (10^9 -10^{10}) cm^3, and local thermalization times on the order of a few seconds, near the limb of the Sun; thus, it is reasonable to speak of a single temperature of the plume plasma at the low altitudes imaged by EIT.

The most remarkable temporal characteristics of the plumes are their constant change on the small scale and their static nature on larger scales. Figure 4 shows several images and a light curve of the two plumes near the center of Figure 2. The shape of each plume's core changes dramatically on a time scale of less than 10 min, with small filamentary structures ($\sim$5 arc sec across) brightening and fading apparently randomly. These intensity variations amount to $\sim$10% of the plume's background-subtracted brightness, and propagate coherently outward at speeds of 300$-$500 km s^{-1}. The propagation speed is near the estimated Alfvén speed, suggesting some type of compressional waves possibly driven by small, impulsive events at the base of the plume. A more detailed time-domain analysis is being performed by DeForest and Gurman (1997).

On time scales of hours to days, and spatial scales of $>$30 arc sec, the observed plumes' overall shapes appear fixed: we observed little or no change in the plumes' large-scale shapes over the course of the 16-hour observation, and the brightest plumes maintained the same overall structure in the EIT images as early as one day before and as late as one day after the main high cadence sequence. However, plumes may change their overall intensity rather suddenly: several 'plumewise

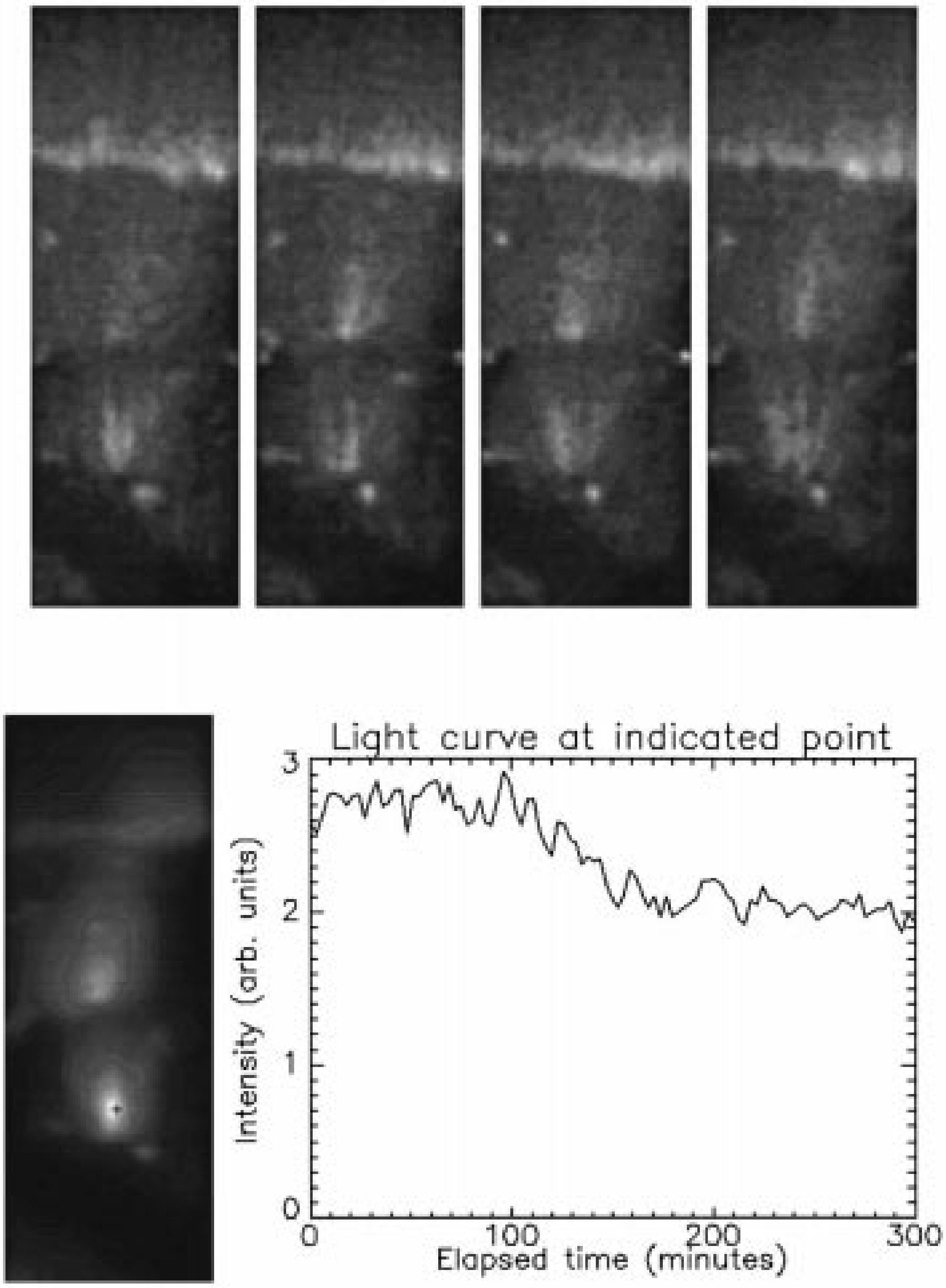

Figure 4. Time variability of EIT images. *Top*: a sequence of four frames, taken 9 min apart, of the two bright plumes at the center of Figure 2 in the EIT Fe IX/X (171 Å) band. A radially-varying model background corona has been subtracted from the images. *Bottom*: a time-averaged image of the above two plumes for all five hours (104 frames) of the high-cadence period. The frames have been translated and rotated in the image plane to keep the lower plume stationary (causing some registration error, hence blurring, in the upper plume). The graph at right shows intensity variation at the marked '+'. The fluctuation amplitude is ∼20%; this is ∼10 times the noise level in the individual images.

global' events were observed, in which a whole plume permanently changed its Fe IX/X brightness by up to a factor of 2 over a span of ∼2 hours, without significantly changing shape.

2.2. MDI: MAGNETIC FOOTPOINTS OF PLUMES

MDI (Scherrer *et al.*, 1995) recorded high-resolution mode (0.6 arc sec pixel) magnetograms, Dopplergrams, and line-depth images of the photosphere in the Ni I 6768 Å absorption line. Figure 5 shows two views of a single south pole magnetogram made by averaging 5 min worth of data. The top is scaled so that black and white correspond to ± 200 G along the line of sight; the second is scaled to show the details of the weaker field structure. The line-of-sight field has been divided by the cosine of the surface projection angle, giving an estimate of the radial field at each point; this is why the region near the limb of the Sun appears 'noisier' than the regions farther away. The most apparent feature in the upper image is the magnetic flux concentrations that dot the surface of the Sun. The chief difference between the coronal hole and 'quiet-Sun' regions in this image is the presence (outside the coronal hole) or lack (within the coronal hole) of balance in the strength of the flux concentrations of opposing sign.

Figure 6(A) shows the distribution of field strength by percentile pixel value in the boxed region in Figure 5. The strongest flux concentrations in the coronal hole, which account for ∼2% of the covered area, have a peak radial field strength of ∼300 G (the average field inside the flux concentrations depends on how the boundaries of the concentrations are treated). The net average field into the indicated region is ∼5 G. The r.m.s. line-of-sight weak field (outside the flux concentrations) is ∼8 G (with the instrument's inherent 0.6 arc sec pixel averaging); after binning the image into 1.2 arc sec pixels, the r.m.s. line-of-sight weak field is 3.5 G.

The flux concentrations account for about half of the magnetic flux that escapes the coronal hole. Figure 6(B) shows the average flux through the boxed region in Figure 5 when the strongest pixels (white and black) are removed. Neglecting the strongest 5% of the image area removes half of the total net magnetic flux.

Figure 7 is an example of an MDI image that is co-aligned with, and overlain upon, a simultaneous EIT image in 171 Å light. The two images have been scaled to the same resolution, and regions of the EIT image where the measured line-of-sight magnetic field was stronger than 20 G were replaced with the MDI signal, in blue (negative; white in Figure 5) or red (positive; black in Figure 5). Several plumes are visible. Every plume that lands on a place that is visible in the magnetogram (i.e., not closer than ∼1 arc min to the limb) lands on a unipolar magnetic flux concentration. The relationship is not one-to-one: not all of the flux concentrations are plume footpoints.

The finding that plume footpoints occur on unipolar magnetic flux concentrations permits one to understand the geometry of the lowest portion of the plume in terms of the magnetic field configuration (as in Newkirk and Harvey, 1968):

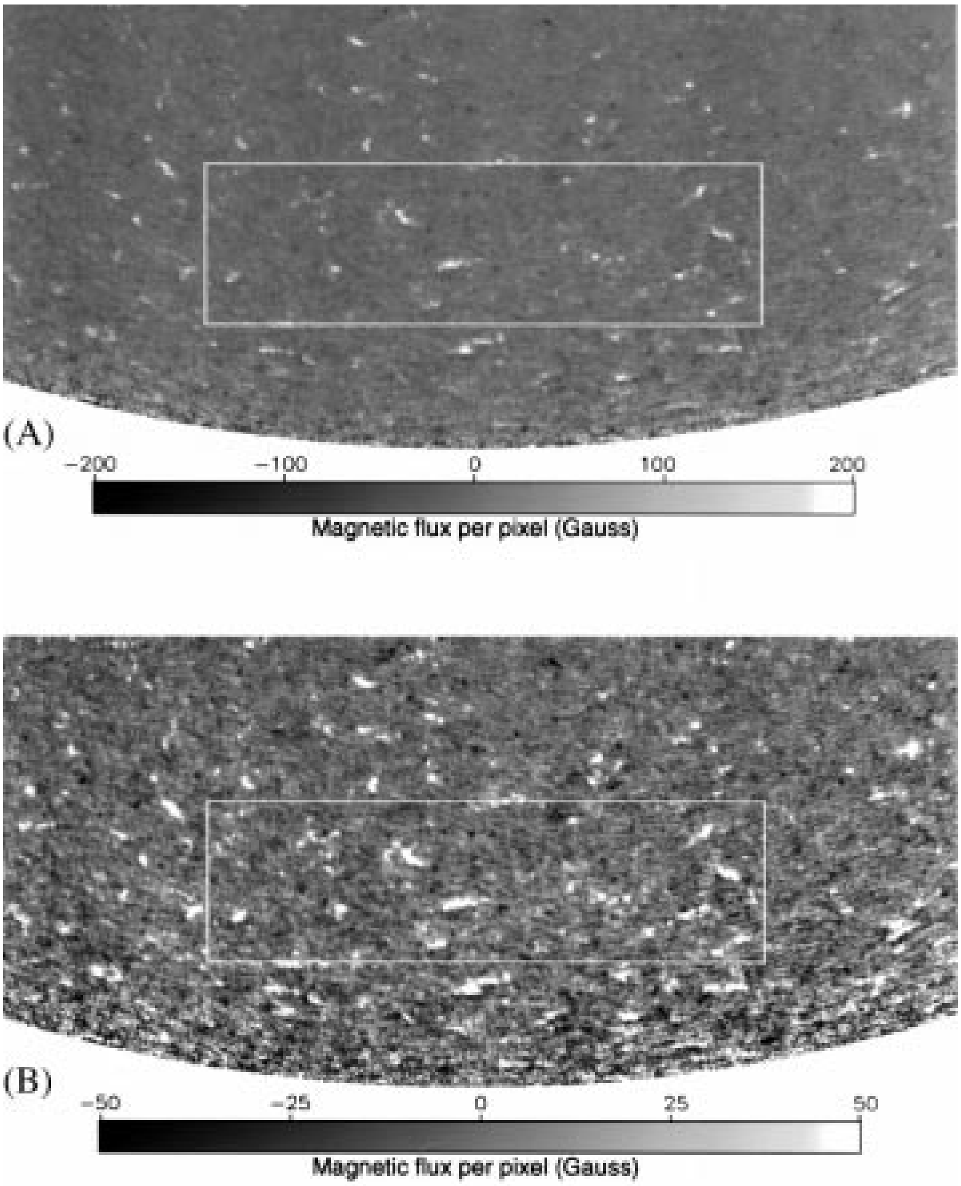

Figure 5. MDI high-resolution magnetogram showing the flux concentrations in the coronal hole. (A) This image has been scaled so that the brightest spots (±200 G along the line of sight) are black/white, to illustrate the details of the strong field. (B) This image has been scaled to ±50 G to illustrate the weak background field outside the stronger flux concentrations. The white rectangle marks the region used to generate the plots in Figure 5. Both images have been adjusted for the projection angle of local vertical into the line of sight.

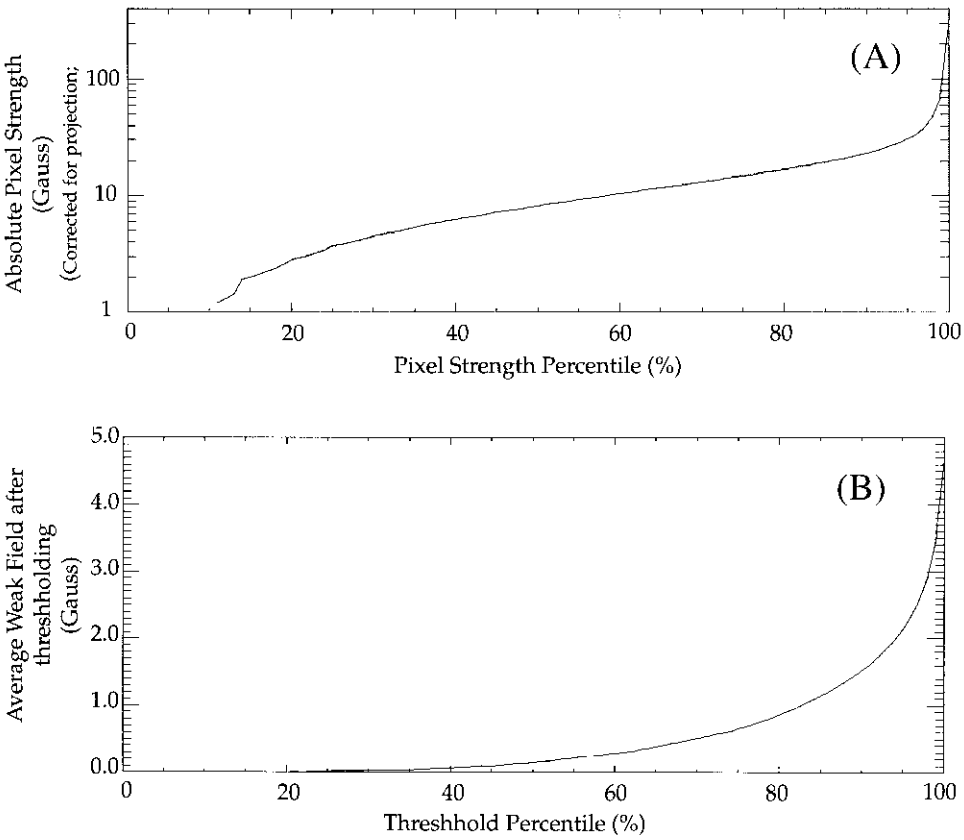

Figure 6. Statistical breakdown of measured line-of-sight magnetic flux within the white rectangle in Figure 4. The top plot (A) shows the distribution of absolute angle-corrected field strength vs percentile. Only a small percentage of the pixels have values >30 G. The lower plot (B) shows the calculated average field over the whole region, when the strongest pixels are removed from the average. The strongest 5% of the pixels account for over half of the average field.

assuming a density of $\sim 10^{10}$ cm^{-3} (Walker *et al.*, 1993) and electron temperature of 10^6 K inside the base of a plume gives (in a 100 G magnetic field) a plasma β parameter of 4×10^{-3}, so that plume geometry should be close to the shape of a force-free field. Suess *et al.* (1997) have extensively modelled polar plume expansion in the potential-field geometry; the principal limitation of the initial superradial expansion is the presence of other open magnetic field lines (either from a smooth background field or other magnetic flux concentrations).

The footpoints that give rise to plumes appear to be more complex than the ones that do not give rise to plumes. For example, the two central plumes in Figure 7 both have complicated footpoints with several local maxima of field strength. Several equally strong but morphologically simpler concentrations are visible in Figure 7; and these flux concentrations do not appear to give rise to plumes.

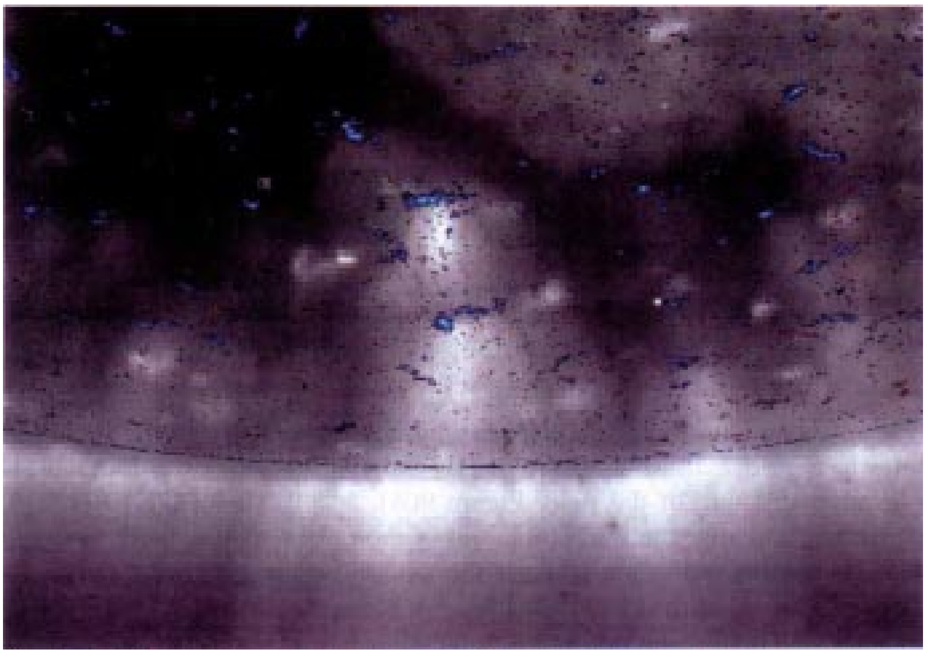

Figure 7. Overlay of an MDI magnetogram with a simultaneous image from EIT in Fe IX (171 Å). Regions where the photospheric field is strong have been replaced with magnetic information in a blue/red color scheme. Fields between −20 and +20 G are not visible; the colored spots are graded in intensity from 20 to 160 G (uncorrected) along the line of sight in each direction. Each polar plume whose footpoint is visible lands on a unipolar blue flux concentration. The brightest plumes appear to arise from flux concentrations with more complex geometry; however, in no case does a plume footpoint correspond to a balanced dipole magnetic structure.

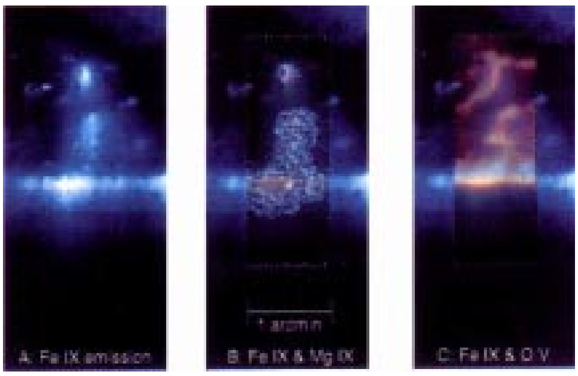

Figure 8. Plume footpoints as seen by EIT and CDS. (A) The central region of Figure 3(A), showing the footpoints of the two central plumes in Fe IX emission (171 Å), as seen by EIT. (B) Overlay of a simultaneous CDS image in Mg IX light (368 Å; contours) with (A). The plumes and the limb of the Sun are congruent between the two images. (C) Overlay of a simultaneous CDS image in O V (629 Å; orange color table) with (A). The plumes are visible but appear orange as they ‘shine through’ the orange color table of the O V. The plume footpoints are on the chromospheric network (on cell boundaries); however, there is nothing in the O V image to distinguish the plumes’ footpoints from other parts of the network.

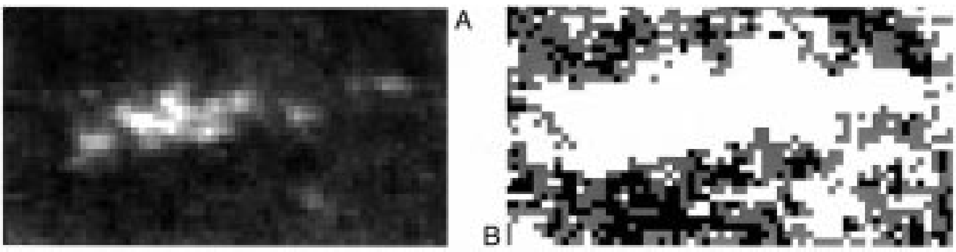

Figure 9. Magnetogram close-up of a plume footpoint as seen by MDI. (A) The footpoint of the brightest plume in Figure 7 (near the center of the image). (B) Mask indicating where the field is within one sigma of zero (grey); into the page (white); or out of the page (black).

Figure 9 is a close-up of the flux concentration under one of the two central plumes in Figure 7, illustrating the mainly unipolar nature of the footpoint and the detailed structure of the field. Figure 9(A), at left, shows the several local maxima that comprise the main footpoint of the plume; Figure 9(B), at right, is a three-level mask indicating whether the field is positive, within 8 G (i.e., one standard deviation) of neutral, or negative. For scale, the squares in Figure 9(B) are individual MDI high-resolution pixels, subtending 0.6 arc sec each. Note that, while there are weak opposing-flux regions near the base of the plume, there is no overall dipole nature to the footpoint. The total measured, radial-projection-corrected flux into regions that are white in Figure 9(B) is 8.6×10^{19} Maxwells; the flux into the black regions is -9.5×10^{18} Maxwells, or about an order of magnitude less than the forward flux.

2.3. CDS: PLUME FOOTPOINT LOCATION IN THE CHROMOSPHERIC NETWORK

The two central plumes in Figure 2 were within the CDS field of view, allowing the plumes' footpoints to be located relative to chromospheric features as seen in the He I (584 Å) and O V (629 Å) emission lines (Harrison *et al.*, 1995). CDS acquired intensity data in its three brightest lines, the He I, O V, and Mg IX (368 Å) lines for a period of 1 hour near and following 17:00 UT on 7 March 1996.

Figure 8(A) shows the central portion of the EIT field of view; Figure 8(B) shows the same image, with simultaneous CDS Mg IX intensity contours overlaid upon it. Mg IX and Fe IX are present at approximately the same temperature. The two central plumes are visible in the CDS Mg IX data, and their shape agrees well with the EIT image.

Figure 8(C) is a similar overlay, with Fe IX in blue-white and O V in orange–white. The plumes' footpoints clearly land within the chromospheric network, on the boundaries of network cells. This is in agreement with the observation that plumes arise from magnetic flux concentrations: magnetic flux has been shown by Berger and Title (1996) to be carried rapidly to the edges of network cells by normal supergranular convection.

While the plumes seem to land on bright portions of the chromospheric network, there is no distinguishing characteristic of those particular brightenings in the CDS images: there are many small brightenings visible in the images, and without the Fe IX overlay, it is impossible to determine where the footpoints lie.

2.4. MK-3 AND LASCO: OUTER STRUCTURE OF PLUMES

Coronal rays, the linear structures visible in the polar coronal holes with white-light coronagraphs, have been studied extensively (see, for example, Fisher and Guhathakurta, 1995; Newkirk and Harvey, 1968). The rays are density structures that are visible in Thomson-scattered white light in the low to mid corona. To compare near-simultaneous coronal rays and plumes, and to trace the plumes out as far as possible, the LASCO coronagraph (Brueckner *et al.*, 1995) acquired white-light brightness images of the corona in its C2 (2 $R_\odot$–6 $R_\odot$) and C3 (5 $R_\odot$–30 $R_\odot$) telescopes. Because the spacecraft off-point during the campaign required LASCO to shut its doors (due to concerns about direct solar exposure past the occulters), LASCO images were not taken during the high cadence portion of the campaign. A complete set of images was recorded before the spacecraft pointing was initially adjusted, and again after it had returned to the nominal direction.

The LASCO data are unpolarized white-light images, and thus include Thomson scattered light from the K-corona and specularly scattered light from the F-corona. The F-corona is a slowly-varying signal added onto the K-corona signal; it was removed from the raw C2 and C3 images by subtraction of a radially varying, smooth function that was fit to the radial dropoff in background intensity. The resulting images were subjected to more traditional radial filtering (in which they were multiplied by a slowly varying function of radius) to raise the contrast near the outer edges of the images.

Coronal rays were clearly visible over the South pole in the processed C2 and C3 white-light images. The Mk-3 daily average images from 7 and 8 March were co-aligned with the SOHO instruments' images to bridge the gap between the LASCO C2 field of view ($>$2.0 $R_\odot$) and the EIT field of view ($<\sim$1.3 $R_\odot$); and to allow a detailed comparison of the white-light rays and the XUV plumes.

Unfortunately, bad seeing conditions at MLSO on 7 March raised the noise level of that day's images above the intensity level of the rays, so simultaneous image comparisons are not possible between the SOHO and the Mk-3 data. Instead, we use the Mk-3 image from 8 March (mean time 22:00 UT 8 March 1996), whose collection time is some 16 hours later than the last SOHO images from the campaign.

Figure 10 is a montage image made by co-aligning images from EIT (171 Å), Mk-3 (white-light polarization brightness, daily average), and LASCO's C2 camera, showing fair to good correspondence between the plumes (in EIT) and the rays (in Mk-3 and LASCO). We identify the XUV polar plumes seen in EIT with the coronal rays seen by Mk-3 and LASCO. The slight positional mismatches are

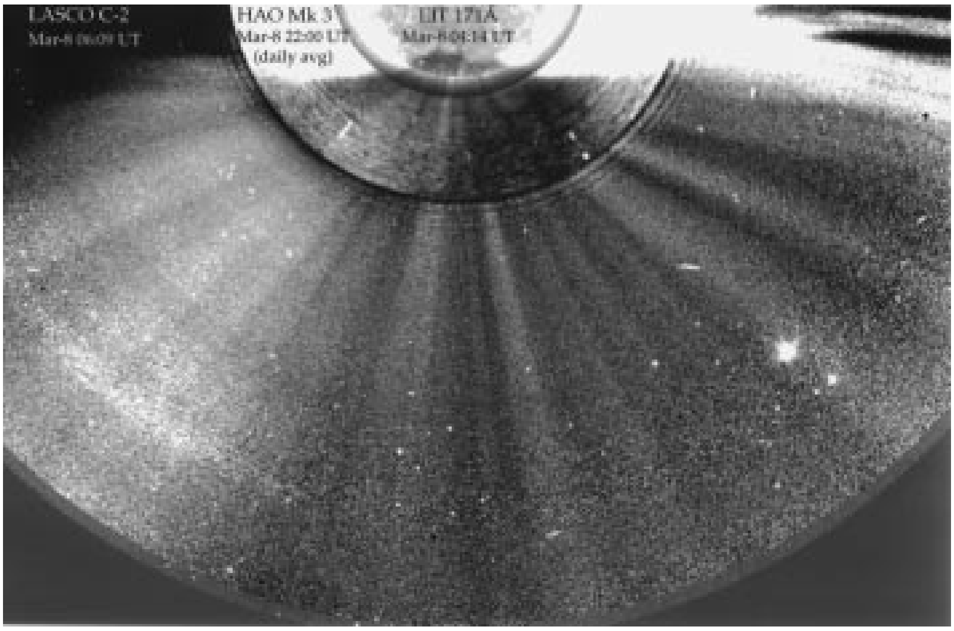

Figure 10. Embedded images of the corona as seen by EIT (Fe IX/X line emission), the MLSO Mk-3 white-light coronameter (white-light polarized brightness), and LASCO's C2 camera (unpolarized white light). The two outer images have been subjected to radial filtering. Despite the 16-hour difference between the Mk-3 and SOHO data collection times, there is good correspondence between plumes observed in the three fields of view.

attributed to solar rotation during the 16-hour time difference between the Mk-3 and the other two images: the plumes whose projection angle out of the image (as determined by footpoint location) is small match the Mk-3 better than the ones whose projection angle is large; and the apparent mismatches go in opposite directions between EIT–Mk-3 and Mk-3–C-2.

We find that the plumes/rays appear to diverge radially from a point that is between the solar center and the South pole of the Sun; this agrees with the observations of Fisher and Guhathakurta (1995) with SPARTAN data and DeForest (1995) with the Stanford/Marshall Space Flight Center Rocket Spectroheliogram.

To clarify the expansion behavior of the observed plumes, and to fit the huge LASCO C3 field of view into the same figure with EIT, it was necessary to transform the plume images into radial coordinates. Figure 11 presents the same data as Figure 10, but extended into the LASCO C3 field and mapped into image-plane radial coordinates. The transformation preserves the shape of small features (such as plume footpoints), and directly represents a feature's subtended linear angle relative to disk center in the image plane. For example, the coronal hole subtends approximately 50° at the limb of the Sun (near the bottom of the image); but expands to subtend closer to 150° by 3 $R_{\odot}$. Straightness of lines is not preserved: Figure 10, which is in Cartesian image coordinates, shows that the rays appear

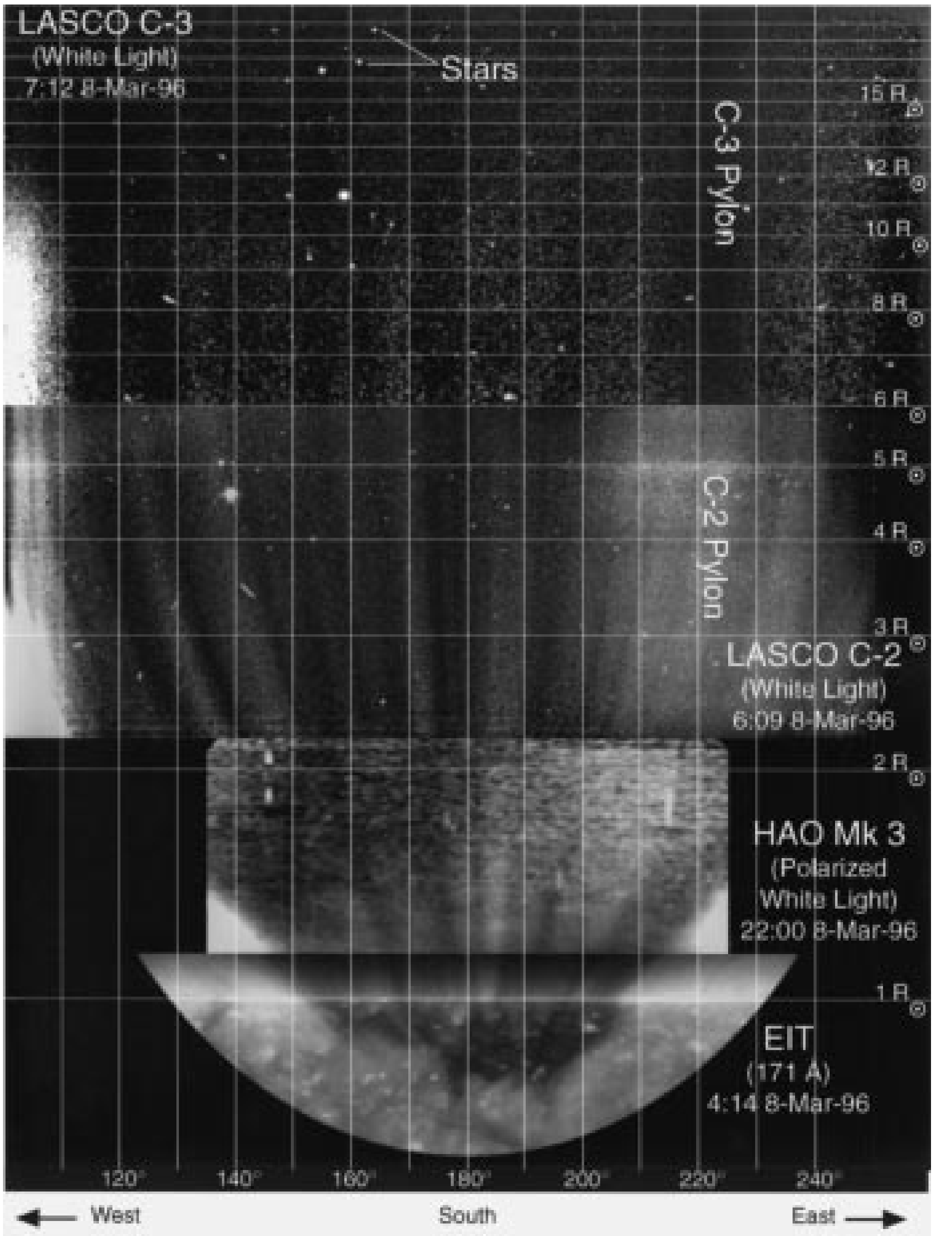

Figure 11. Overlain images of the data in Figure 10 and an image from the LASCO C3 camera, in an image-plane radial coordinate system. Circles concentric with the solar disk have been mapped to horizontal lines; lines radial to the Sun have been mapped to vertical lines. (Note that lines that are radial in 3-space are also radial in 2-D projection.) The superradial expansion of the coronal hole, and of individual plumes, can be seen directly in this image. The logarithmic scaling of radius renders the coordinate transformation 'conformal', meaning that the shape of small features is preserved though scale changes with altitude.

straight; in the transformed image, they appear curved. All three of the visible light coronagraph images have been subjected to radial filtering and/or background subtraction; however, none of the images has been treated with generic unsharp masking. In particular, great care has been taken only to introduce radial (and not angular) gradients, so as to preserve the apparent size and position of the plumes at all altitudes. The C3 image has been divided by a modelled vignetting function that varies only near the marked pylon.

Fisher and Guhathakurta (1995) found that rays observed by SPARTAN appear to expand radially, subtending the same 2.5-deg angle relative to Sun center, regardless of altitude; the LASCO data are not consistent with that observation. We find that, above the rapid-phase expansion at the footpoint, plumes expand superradially in two broad phases outside the image-plane solar limb. The difference in the two phases lies in the comparison between the plumes' expansion ratio and the global expansion ratio of the coronal hole. In the lower phase, below 5 $R_\odot$, the plumes and the coronal hole expand at roughly the same rate. Above about 5 $R_\odot$, the coronal hole has expanded to fill nearly the entire hemisphere (as the streamer belts pinch off), and begins to expand radially. However, the brightest plumes in Figure 2 continue to expand superradially between 5 $R_\odot$ and 15 $R_\odot$, where they fade into the background noise of the C3 image. The FWHM of a typical bright plume is 2.5° at 1.05 $R_\odot$; $\sim$7° at 5 $R_\odot$; and $\sim$15° at 15 $R_\odot$, for a linear expansion ratio of 1, $\sim$3, and $\sim$6 at the three altitudes. Over the same altitude range, the coronal hole expands from 50° on the limb to 150° at 5 $R_\odot$ and 160° at 15 $R_\odot$, for a linear expansion ratio of 1, 3, and 3 at the three altitudes.

3. Conclusions

Combining the data from several SOHO instruments has resulted in a coherent picture of polar plumes by allowing a complete 'snapshot' of a particular set of the plumes to be recorded. Plumes originate in unipolar magnetic flux concentrations that lie on cell boundaries in the chromospheric network. They expand rapidly superradially (with a half-cone angle of $\sim$45°) in their lowest 20–30 Mm, and more slowly above that, for a linear superradial expansion factor of 3 at 4–5 $R_\odot$ and of $\sim$6 at 15 $R_\odot$. Plumes (as seen in XUV) are density structures that are also seen as coronal rays (in Thomson-scattered white light) in the mid to upper corona. They are denser than the surrounding media (as observed by Walker *et al.*, 1993) and are discernable to an altitude of at least 10–15 $R_\odot$. In their lower reaches, plumes are slightly cooler than the surrounding interplume coronal hole, by a factor not exceeding $\sim$30%. On distance scales of $>$15 arc sec, plumes are remarkably quiescent structures, maintaining their form essentially unchanged for days at a time; at smaller distance scales, they exhibit outward flowing fluctuations in density and/or temperature on a time scale of a few minutes and a length scale of $\sim$5–15 arc sec, up to an altitude of at least 1.2 $R_\odot$.

4. Direction of Future Analyses

Several of the results presented here lend themselves to continued study. Because this observing campaign was run during SOHO's commisioning phase, several of the instruments in the SOHO plumes campaign had not yet been absolutely calibrated; detailed analysis has had to wait for the final calibration. In particular, derived densities and temperatures (e.g., DeForest, 1995) from the EIT data in the lower corona will be important for comparison with past results. Likewise, a detailed intercomparison of line width temperatures from SUMER and ionization state temperatures from EIT should be made. That work is in progress, and is currently awaiting absolute intensity calibrations from EIT.

Suess *et al.* (1997) have developed detailed models of the magnetic structure inside coronal holes, which should be compared with the actual morphology at the footpoints of plumes seen in EIT. Suess's model includes rapid flux tube expansion with altitude above flux concentrations; the flux tube expansion is limited by the total background field. Comparing plume geometry and flux concentration statistics to the model will indicate the proportions of closed field lines emanating both from flux concentrations and the 'quiet coronal hole' in between them.

The observed rapid small-scale brightness variation in plumes, coupled with their large-scale stability, is puzzling. A careful comparison of the variations with bulk photospheric motions and/or magnetic field changes at the footpoints may help explain plume heating and acceleration. Ofman and Davila (1997) have proposed a heating model in coronal holes that invokes nonlinear Alfvén-compressional wave coupling in the 5-min frequency band; the correspondence of plumes with the more complicated flux concentrations suggests that plumes may be heated by small magnetic reconnection events at their footpoints. Time domain analysis of the existing data is needed to test these ideas.

Acknowledgements

Participation in this observation has been broad-based, and many individuals not named on the author list have contributed to the observation and analysis described by this article. Special thanks are due to the principal investigators of the SOHO instruments, for allowing this science campaign to be run during SOHO's commissioning period; and to the flight operations teams of the spacecraft and of the individual instruments. Stanford's Rick Bogart initially pointed out the possibility of an MDI polar high-resolution campaign during the SOHO commissioning phase. Giannina Poletto and Steve Suess provided insightful commentary and conversation on plume and magnetic field structure; Madhulika Guhathakurta and Dick Fisher helped understand the data from the HAO instrument.

SOHO is a project of international co-operation between NASA and ESA.

References

Ahmad, I.A. and Webb, D. F.: 1978, *Solar Phys.* **58**, 323.
Ahmad, I. A. and Withbroe, G. L.: 1977, *Solar Phys.* **53**, 397.
Allen, M. J.: 1994, 'The First Flight of the MSSTA', doctoral dissertation, Stanford University.
Berger, T. E. and Title, A. M.: 1996, *Astrophys. J.* **463**, 365.
Bohlin, J. D., Sheeley N. R., Jr., and Tousey, R.: 1975, in M. J. Rycroft (ed.), *Space Research XV*, Akademie-Verlag, Berlin, p. 651.
Brueckner, G. E. *et al.*: 1995, *Solar Phys.* **162**, 357.
Delaboudinière, J.-P. *et al.*: 1995, *Solar Phys.* **162**, 291.
DeForest, C. E.: 1995, 'High Resolution Multi-Spectral Observations of Solar Coronal Open Structures: Polar and Equatorial Plumes and Rays', doctoral dissertation, Stanford University.
DeForest, C. E. and Gurman, J. B.: 1997, *Astrophys. J.*, in press.
DeForest, C. E. *et al.*: 1990, *Opt. Eng.* **30**, 1126.
Fisher, R. and Guhathakurta, M.: 1995, *Astrophys. J.* **447**, L139.
Fleck, B., Domingo, V., and Poland, A. I. (eds): 1995, *Solar Phys.* **162**.
Habbal, S. R.: 1992, *Ann. Geophys.* **10**, 34.
Harrison, R. A. *et al.*: 1995, *Solar Phys.* **162**, 233.
Harvey, J. W.: 1965, *Astrophys. J.* **141**, 832.
Hassler, D. M., Wilhelm, K., Lemaire, P., and Schuehle, U.: 1997: *Solar Phys.*, in press.
Koutchmy, S.: 1977, *Solar Phys.* **51**, 399.
Lindblom, J. F.: 1990, 'Soft X-Ray/Extreme Ultraviolet Image of Solar Atmosphere with Normal Incidence Multilayer Optics', doctoral dissertation, Stanford University.
Newkirk, G., Jr., and Harvey, J.: 1968, *Solar Phys.* **3**, 321.
Ofman, L. and Davila, J. M.: 1997, *Astrophys. J.* **476**, 357.
Saito, K.: 1965, *Publ. Astron. Soc. Japan* **17**, 1.
Scherrer, P. H.: 1995, *Solar Phys.* **162**, 129.
Suess, S. T.: 1982, *Solar Phys.* **75**, 145.
Suess, S. T., Poletto, G., Wang, A.-H., Wu, S. T., and Cuseri, I.: 1997, *J. Geophys. Res.*, submitted.
Walker, A. B. C. *et al.*: 1988, *Science* **241**, 1781.
Walker, A. B. C., DeForest, C. E., Hoover, R. B., and Barbee, T. D. W.: 1993, *Solar Phys.* **148**, 239.
Wang, Y.-M.: 1994, *Astrophys. J.* **435**, L153.